A Dynamic Calibration Method for Pirani Gauges Embedded in Fluidic Networks

Seungdo An, *Member, IEEE*, and Yogesh B. Gianchandani, *Fellow, IEEE*

***Abstract*— This paper describes *in situ* dynamic calibration of microfabricated Pirani gauges, which are commonly used to measure vacuum levels in microsystems that may include pumps, valves, and other pressure modulation elements. Calibration is accomplished with a configuration where two sides of the supporting membrane of a Pirani gauge are at different pressures: an interior pressure within the microsystems and an exterior ambient pressure that can be directly controlled. This particular configuration is increasingly common as Pirani gauges are embedded in complex fluidic pathways such as those found in micro-gas chromatographs and multistage gas pumps. In the dynamic calibration the ambient pressure is rapidly modulated, while the interior pressure in the sense gap of the Pirani gauge remains relatively unchanged. The exterior pressure that is equal to the interior pressure is determined by a regression model. The dynamic calibration procedure and subsequent error analysis are illustrated by application to a 162-stage monolithic Knudsen vacuum pump. For this device, dynamic calibration improves the estimated upstream pressure from 30 (as suggested by uncorrected static calibration) to 0.9 Torr, with a 95.4% confidence interval from 0.7 to 1.1 Torr, assuming normal (Gaussian) distribution. These results demonstrate that dynamic calibration can be significantly more accurate than conventional static calibration for certain types of devices. [2013-0139]**

***Index Terms*— Pirani gauge, pressure sensor, dynamic calibration, static calibration.**

I. Introduction

PIRANI gauges, which transduce gas pressure into changes in electrical resistance [1]–[3], have been widely used in microsystems [4]–[14]. Typically, the Pirani gauge has a resistive heating element that is suspended on a thermally isolated membrane. The heat generated in the operation of the Pirani gauge flows across a sense gap beneath the membrane, to a substrate, which serves as the heat sink. As the vacuum level or gas pressure changes in the sense gap, the resulting change in thermal conductance causes a change in the temperature of the membrane (or alternatively, a change in the power level necessary to maintain it at a fixed temperature). The change in temperature can be detected by the resistive heating element, or alternatively by another resistor. The structure and operation of a typical Pirani gauge are illustrated in Fig. 1. Pirani gauges

Manuscript received April 30, 2013; revised August 27, 2013; accepted September 6, 2013. This work was supported in part by the Microsystems Technology Office of the Defense Advanced Research Projects Agency High-Vacuum Program under Contract W31P4Q-09-1-0011. The work of S. An was supported in part by a fellowship from the Electrical Engineering and Computer Science at the University of Michigan. Subject Editor C. Liu.

The authors are with the Department of Electrical Engineering and Computer Science, University of Michigan, Ann Arbor, MI 48109 USA (e-mail: sdan@umich.edu; yogesh@umich.edu).

Color versions of one or more of the figures in this paper are available online at http://ieeexplore.ieee.org.

Digital Object Identifier 10.1109/JMEMS.2013.2281319

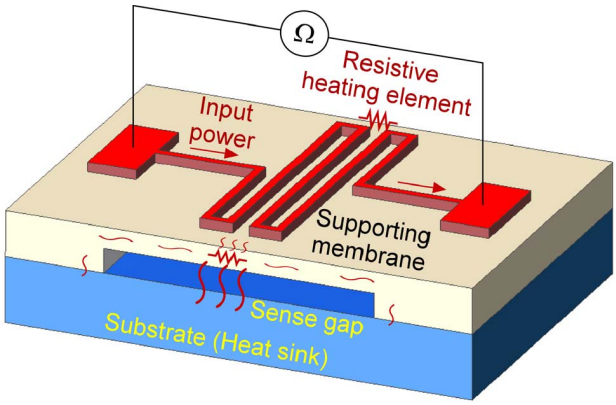

Fig. 1. Schematic of a Pirani gauge.

are favored as embedded sensing elements within microfluidic systems and micromachined pumps [15]–[17], because of simple fabrication requirements that are relatively easy to integrate into other manufacturing processes.

For the accurate measurement of pressure with a Pirani gauge, its resistance variation must be calibrated over the operating pressure range. This is necessary because process-induced sample-to-sample variations in dimensions and material properties can cause variations in the response. A Pirani gauge is typically calibrated by varying the pressure in the sense gap. In most cases, the structure is designed so that the heat loss from the suspended heating element is dominated by thermal conduction through the sense gap; i.e., the heat losses to the exterior of the structure, and the conductive heat losses along membrane on which the Pirani gauge is suspended, are relatively small. During calibration, the interior of the membrane and the exterior of the membrane are both at a common pressure controlled by a calibration pump. In this method, the dominance of the heat loss through the sense gap is retained, and the thermal losses to the exterior [18], [19] are accommodated in the calibration (Fig. 2a). For the purpose of this paper, this calibration procedure is named static calibration. In contrast, when the Pirani gauge resides on a thermally-insulating membrane which completely separates the underlying sense gap from the exterior environment [16], [17], static calibration is likely to be inaccurate because of the lack of direct access to – and control of the pressure in – the sense gap. Further, if the interior pressure is low, the heat losses to the exterior could represent a significant un-calibrated component.

Structures in which the Pirani sense gap is inaccessible are increasingly common in microsystems with complex or tortuous fluidic pathways, such as micro-gas chromatographs

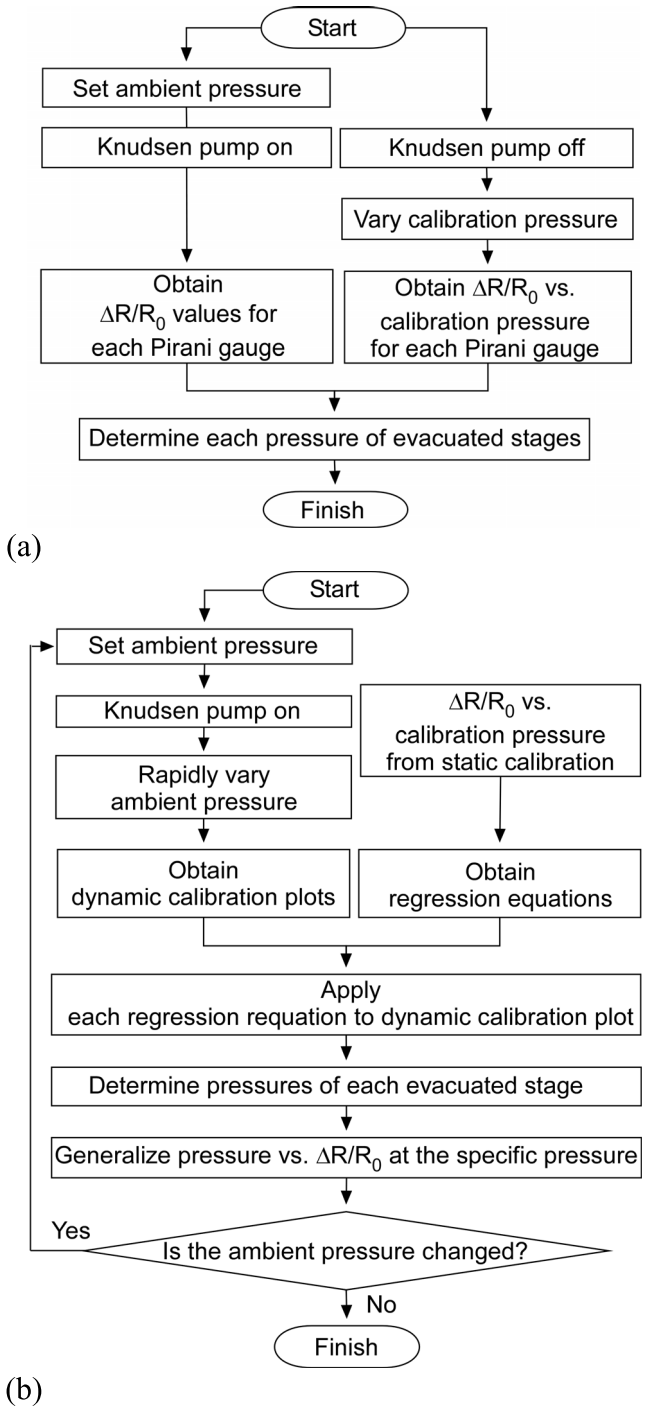

Fig. 2. Flow charts for pressure measurements with Pirani gauges. (a) Using static calibration. (b) Using dynamic calibration.

and multistage gas pumps [20]–[22]. This paper describes a dynamic calibration method used to calibrate Pirani gauges embedded in such structures (Fig. 2b). This method exploits the relative slowness of the pressure variation in a sense gap that is embedded deep within a microfluidic pathway, as compared to the speed with which the exterior pressure can be modulated. The value of the (directly controlled) exterior pressure that is equal to the interior pressure (which is not directly controlled) is determined by a regression model that is fitted to a reference Pirani gauge.

The dynamic calibration method is demonstrated using a Si-micromachined, monolithic 162-stage Knudsen pump [17]. Pirani gauges are embedded within the pump to provide *in situ* pressure measurement at various intermediate points within the flow channel. Each Pirani gauge is positioned next to a pump stage to be measured. The pressure in the sense gap of each Pirani gauge is determined by the Knudsen pump operation, whereas the exterior is at ambient pressure, which is controlled by a calibration pump.

The theoretical operation of the Pirani gauge, the dynamic calibration concept, and the linear regression model are described in Section II. Section III describes the test setup and methodology, followed by the experimental results from the calibration of the sample Knudsen pump by both static and dynamic methods. The possible errors are addressed in estimating the pressure. Conclusions are presented in Section IV.

II. Theoretical Background

This section describes the theoretical considerations for a Pirani gauge in the context of a differential pressure across the supporting membrane. The dynamic calibration is described, followed by the linear regression model of Pirani gauge responses.

A. The Pirani Gauge

As pressure is reduced in the sense gap, the decrease in the density of gas molecules causes an increase in its thermal resistance [3], [5], [6]. The temperature of the supporting membrane and electrical resistance of the temperature-sensing resistor increase as a fixed input current is supplied to the resistive heating element. This development follows the particular case that the heating resistor is also the temperature-sensing resistor, which is the case for the Knudsen pump demonstration of the dynamic calibration method. In this situation, there is an increase in resistance associated with the heating caused by the current used to operate the Pirani gauge. Calibration is specific to the ambient pressure at which it is performed. Therefore, the total electrical resistance, R_T, can be expressed as:

$$R_T = R_0 + R_{0,Ref}(I, P_{Ref}) + \Delta R(I, P_{Cal}) \tag{1}$$

where I is the current; P_{Ref} is the reference ambient pressure; P_{Cal} is the calibration pressure, the pressure of interest lower than P_{Ref}; R_0 is the unheated resistance; $R_{0,Ref}$ is the increment in resistance at P_{Ref}; and ΔR is the further increment in resistance at P_{Cal}. For the purpose of this paper, I and P_{Ref} are fixed at 4 mA and 760 Torr, respectively, for reasons explained in Section III. In constant current mode, the total electrical resistance, R_T, is provided by [23]:

$$\frac{R_T - R_0}{R_0} = \frac{\alpha I^2 R_0 \Re_{th}}{(1 - \alpha I^2 R_0 \Re_{th})} \tag{2}$$

where $\Re_{th}$ is the equivalent thermal resistance of the Pirani gauge, which is a function of pressure. The temperature coefficient of the heating/sensing resistor is denoted by α; for a 25/100 nm Ti/Pt thin film, such as used in the sample Knudsen

pump, its value is 2,314 ppm/K. The thermal resistance, $\Re_{th}$, is the parallel combination of the constituent thermal resistances:

$$\Re_{th}^{-1} = \Re_{d}^{-1} + \Re_{sg}^{-1} + \Re_{ext}^{-1} \tag{3}$$

where $\Re_d$ is the thermal resistance of the supporting membrane, $\Re_{sg}$ is the pressure-dependent thermal resistance of the sense gap and $\Re_{ext}$ is the equivalent thermal resistance to exterior ambient. However, $\Re_{ext}^{-1}$ can be neglected, assuming $\Re_{ext}$ is large relative to $\Re_d$ and $\Re_{sg}$. Using the thermal conductivity equation in [15], the $\Re_{sg}$ is written as:

$$\Re_{sg} = \frac{1}{\sigma_{0,air,th}} \frac{g + 2\lambda(2/a_T - 1)}{A_{heater}} \tag{4}$$

where $\sigma_{0,air,th}$ is the thermal conductivity of air in continuum flow regime, 0.026 K/m/W [24], a_T is the thermal accommodation coefficient (0.75 for air on bright platinum at 280 K [25]), λ is the mean free path of air molecules, which is proportional to temperature and inversely proportional to pressure [26], g is the Pirani sense gap between the supporting membrane and the heat sink, and A_{heater} is the area of the Ti/Pt metal heater. If the pressure within the sense gap is high, $\lambda \ll g$, $\Re_{th}$ becomes nearly equal to $\Re_{sg}$. In contrast, if $\lambda \gg g$, $\Re_{th}$ becomes nearly equal to $\Re_d$. Between these two limits, the fractional change in resistance, caused by the variation in $\Re_{th}$ with pressure, is experimentally characterized in calibration and is used for pressure measurement. At the reference pressure, assuming that the mean free path of the gas molecules is small, i.e. $\lambda \ll g$, the $\Re_{th}$ is approximately equal to the thermal resistance of the sense gap:

$$\Re_{th,Ref} \approx \frac{1}{\sigma_{0,air,th}} \frac{g + 2\lambda_{Ref}(2/a_T - 1)}{A_{heater}} \tag{5}$$

where $\Re_{th,Ref}$ is the thermal resistance at the reference pressure and λ_{Ref} is the mean free path of air molecules at the reference pressure ($\approx$0.07 μm).

The response of greatest interest is $\Delta R/R_0$, which can be correlated to the calibration pressure. Based on Eq. (1-2), it can be written as:

$$\Delta R/R_0 = \frac{\alpha I^2 R_0 \Re_{th}}{(1 - \alpha I^2 R_0 \Re_{th})} - \frac{\alpha I^2 R_0 \Re_{th,Ref}}{(1 - \alpha I^2 R_0 \Re_{th,Ref})} \tag{6}$$

where the second term on the right side is $R_{0,Ref}/R_0$. When the applied current, I, is small (i.e, the denominators on the right side of Eq. (6) are close to 1), the $\Delta R/R_0$ is linearly proportional to the increment in thermal resistance from $\Re_{th,Ref}$. However, as the applied current is increased, the drop in the values of denominators introduces non-linearity in $\Delta R/R_0$. This non-linearity affects the linear relation of $\Delta R/R_0$ to the increase in thermal resistance with pressure, and varies between different Pirani gauges; this is addressed in Section II.D and Appendix A.

B. Mechanical Deformation Caused by Unequal Pressures

If the pressure in the sense gap is smaller than the ambient pressure, it may lead to a deflection of the supporting membrane that decreases the sense gap, thereby decreasing $\Re_{th}$, as indicated by Eq. (4). The ensuing smaller fractional change in electrical resistance indicates higher pressure than the true pressure in the sense gap. The error would be increased by any mechanical contact of the supporting membrane to the substrate as a result of the deformation. The mechanical deformation of the supporting membrane in the sample Knudsen pump is addressed in Section III.

C. Dynamic Calibration

Figure 2b describes the steps in the dynamic calibration of a Pirani gauge. The Pirani gauge to be measured and calibrated is assumed to be embedded deep within a microfluidic pathway, well-separated from the outlet (OUT port, see Fig. 3a). Its supporting membrane separates the Pirani sense gap from ambient pressure. In the steady state condition, an internal pump—a Knudsen pump in this example—maintains the pressure in the sense gap, and an external calibration pump controls the ambient pressure. A second Pirani gauge, the reference gauge, is designed such that both sides of its supporting membrane are at ambient pressure. The rapid modulation of the ambient pressure across a series of values is used to identify an ambient pressure (the equalization pressure) at which the responses of both Pirani gauges are equivalent. In the 162-stage Knudsen pump, a Pirani gauge located at the outlet of the pump is used as the reference gauge.

During calibration, the ambient pressure is modulated in multiple steps. Each step provides a response from the reference gauge that is either greater or less than the responses from the gauge to be calibrated. By interpolating between responses from both gauges through successive modulation steps, the ambient pressure is found at which the Pirani gauges have equivalent responses. At this equalization pressure, the thermal resistances of the two Pirani gauges, $\Re_{sg}$, are also identical, and the membranes are undeflected.

In practice, the Pirani gauge responses may vary even under identical pressure conditions because of minor manufacturing variations. This can be corrected using a linear regression method that is explained next.

D. Mapping of the Response of Pirani Gauges With Linear Regression in Dynamic Calibration

Since the responses of the measured and reference Pirani gauges are compared to each other in dynamic calibration, the response of each Pirani gauge to be calibrated is first mapped to the response of the reference Pirani gauge. This mapping, performed using linear regression, is used to account for the process-induced sample-to-sample variations in the responses. Process-induced variations in the metal width, film thickness or material properties can cause the sample-to-sample variations in R_0, $\Re_{th}$, or α. The linear relationship between the responses of Pirani gauges in the sample Knudsen pump is shown in Appendix A.

The linear transformation of the response of each Pirani gauge to the equivalent response of the reference pressure sensor results in the following relationship:

$$\begin{aligned}\log_{10}(P_{m,S,i}) &= \log_{10}(P_{Cal,i}) + \frac{\log_{10}(P_{Cal,i}) - \log_{10}(P_{Cal,i-1})}{(\Delta R/R_0)_{r,i} - (\Delta R/R_0)_{r,i-1}} \\ &\quad \times ((\Delta R/R_0)_{m,S,i} - (\Delta R/R_0)_{r,i})\end{aligned} \tag{7}$$

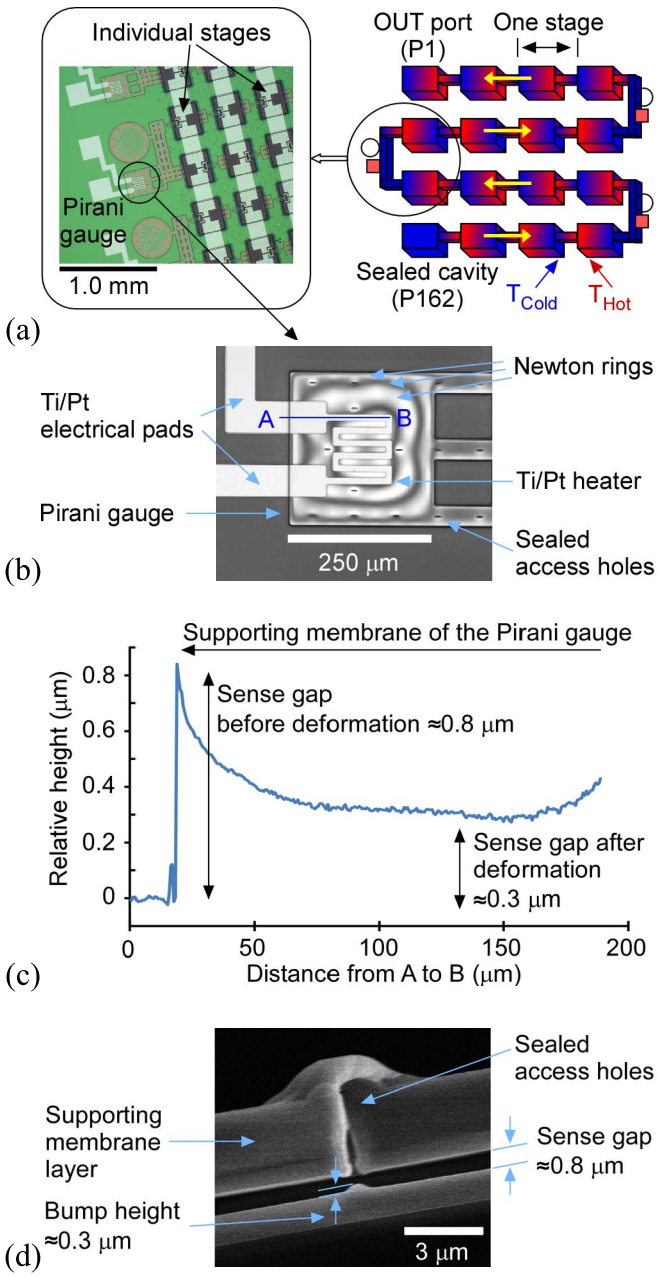

Fig. 3. Sample Knudsen pump and mechanical deformation of the Pirani gauge when the interior pressure is at high vacuum relative to ambient atmospheric pressure. (a) Schematics of multistage Knudsen pump; the left inset shows microscopic photograph of one side of the serpentine multistage structure. (b) Interferogram of a Pirani gauge obtained with a 407 nm laser. (c) Relative height of the exterior surface of the Pirani gauge by interferogram program. (d) Crosssectional SEM photograph of a sealed access hole, when the interior is now at an identical pressure with the exterior.

where $P_{m,S,i}$ is the value converted from the linearly transformed (or scaled) response of the measured Pirani gauge, $(\Delta R/R_0)_{m,S,i}$; i denotes an index value of the calibration pressure, P_{Cal}; or the fractional change in resistance, $\Delta R/R_0$; and the subscripts r and m indicate the reference Pirani gauge and the measured Pirani gauge, respectively. The residual error in pressure, ΔP_E, is defined as the difference between the scaled response and the calibration pressure:

$$\Delta P_{\mathrm{E,i}} = P_{m,S,i} - P_{Cal,i} \tag{8}$$

The linear transformation of each Pirani gauge response to the equivalent response of the reference Pirani gauge is provided by:

$$(\Delta R/R_0)_{m,S,i} = S(\Delta R/R_0)_{m,i} \tag{9}$$

where S is the first-order coefficient (or slope). A practical example is illustrated in Appendix B.

III. Experimental Validation

The experimental validation of the calibration procedure is performed using a 162-stage Knudsen pump, where each stage generates gas flow in the direction of the thermal gradient (Fig. 3a) [17]. Pirani gauges are located at stages 1, 54, 99, and 162, and are named P1, P54, P99, and P162, respectively. Stage 1 is the outlet to the ambient, whereas stage 162 is a blind cavity that is to be evacuated. The chip is wire-bonded, attached to a heat sink, and placed within a test chamber, volume ≈185 L. Ambient pressure is controlled by a rotary pump (Edwards™ E2M30) and monitored, using a commercial calibrated pressure sensor (Adixen™ AHC-2010) located within the test chamber.

The deflection of the supporting membrane of the Pirani gauge is analyzed by interferograms and scanning electron micrographs (Fig. 3). The deflection due to the pressure difference of more than 700 Torr between the interior and the exterior is measured by a laser interferogram (Olympus™ LEXT OLS3100) (Fig. 3b, c). Each Newton ring (bright or dark) represents about a half integer multiple of the laser wavelength (407 nm) in the sense gap (Fig. 3b) [27], [28]. From the relative height of the supporting membrane surface (Fig. 3c), the sense gap in the B region along the A-B line above Ti/Pt metal, after deflection caused by the pressure difference, is ≈0.3 μm. This is smaller than the sense gap of ≈0.8 μm, as shown in the SEM image of the supporting membrane, in the absence of a pressure difference (Fig. 3d). However, this sense gap of ≈0.3 μm is nearly identical to the bump that is created by the sealing layers as they are deposited into the access holes for the sacrificial dry etchant [16] (Fig. 3d). This bump height suggests that the deflected membrane may contact the bump surface so the equivalent thermal resistance of the sense gap could further decrease. The fractional change in resistance caused by the mechanical strain of Ti/Pt metal is negligible in the deflected membrane.

A. Set-Up and Methodology

To select the operating conditions for the Pirani gauges, a preliminary evaluation is performed by varying calibration pressure and input current, using the static calibration method (Fig. 4). A constant current is provided to the Pirani gauges that are connected in series. From the change in $\Delta R/R_0$ with varying calibration pressure, at each current level, it is evident that the responses from 1 Torr to 100 Torr show greater sensitivity than those from 100 Torr to 760 Torr and from 0.1 Torr to 1 Torr. As the current varies from 2.83 mA to 4.90 mA, the $\Delta R/R_0$ and the ΔT are increased, as anticipated by Eq. (6). The fractional change in resistance

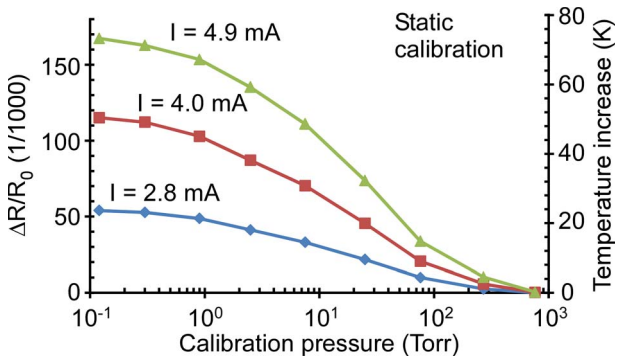

Fig. 4. A preliminary evaluation of a Pirani gauge. The fraction change in resistance and temperature change of a Pirani gauge are investigated as a function of calibration pressure, with increasing current values. The squared value of the current is approximately linear with $\Delta R/R_0$, as shown in Eq. (6). These values are obtained from static calibration.

is approximately proportional to the square of the current. The maximum values of ΔT are 23.4 K for 2.8 mA, 49.9 K for 4.0 mA, and 68.2 K for 4.9 mA. Of these, the current of 4.9 mA provides the highest sensitivity in $\Delta R/R_0$, as can be seen in the plots (Fig. 4). However, in order to reduce the likelihood for thermal aging of the resistor, drift in resistance and non-linearity in fractional change in resistance, an operating current of 4 mA is selected. It is applied to the nominal R_0 of 140 Ω in this test and also to all of the Pirani gauges in the Knudsen pump sample, where the value of R_0 varies from 130 Ω to 150 Ω on a wafer-to-wafer basis.

Using the measured α value of 2,314 ppm/K and the variation in $\Delta R/R$ with the current of 4 mA, the $\Re_d$ value can be estimated for the low pressure limit, with Eq. (6). The second term on the right side of Eq. (6) is characterized as 10.3×10^{-3}, providing the $\Re_{th,Ref}$ value of 2,002 K/W. At 0.12 Torr, the $\Re_d$ value is nearly identical to the $\Re_{th}$ value of 21,826 K/W.

B. Pressure Estimation Using Static Calibration

In static calibration (Fig. 5a), the responses of each Pirani gauge with variations in calibration pressure are obtained, while the Knudsen pump is off (Fig. 5a). For exposing both sides of the supporting membrane in each Pirani gauge to equal ambient pressures, perforations are created close to the calibrated Pirani gauges, thereby enabling the interior pressure to be controlled by the calibration pump. It is that this calibration process is destructive because of the need of these perforations, and is consequently performed after the pumps are tested. As a practical matter, pumps within close proximity are expected to perform similarly, so only a limited number must be sacrificed for calibration.

Each pressure level (Fig. 5b) is calculated by interpolation between the neighboring points in static calibration data (Fig. 5a). Interpolation is performed using straight lines with calibration pressure in log-scale and $\Delta R/R_0$ in linear-scale. To reduce the error from the straight line between the neighboring points, the calibration pressures are closely spaced at half-decade intervals. The $\Delta R/R_0$ value of 4.3×10^{-3} of P54 is mapped to 430 Torr, the $\Delta R/R_0$ value

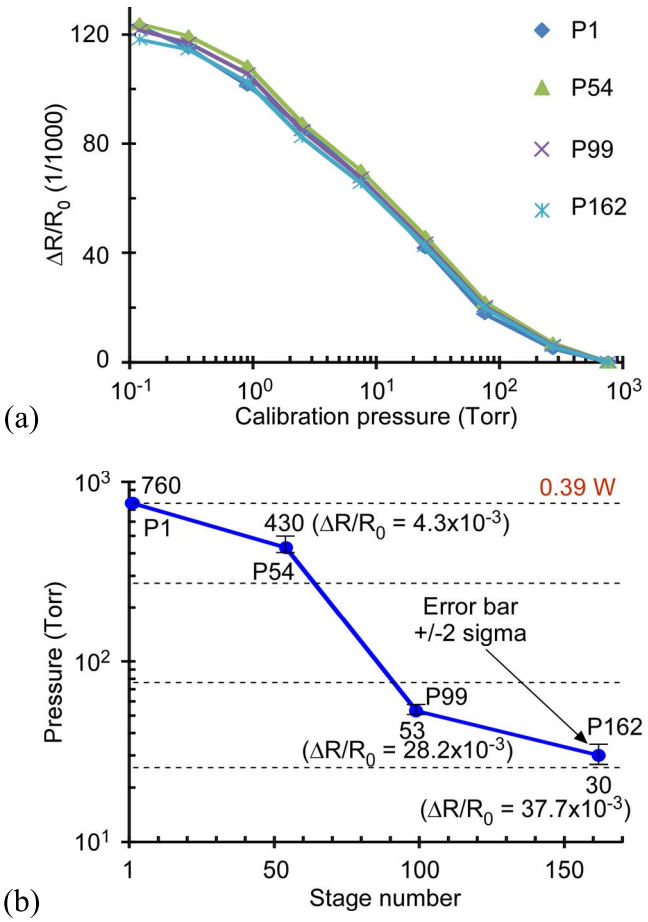

Fig. 5. The pressure levels of the Pirani gauges, using the static calibration of Pirani gauges of P1, P54, P99, and P162. (a) Each response of the Pirani gauges with varying calibration pressure. (b) Each estimated pressure of the Pirani gauges with the Knudsen pump operation. The horizontal dotted lines in (b) are the static calibration pressures which are used for interpolations.

of 28.2×10^{-3} of P99 to 53 Torr, and the $\Delta R/R_0$ value of 37.7×10^{-3} of P162 to 30 Torr. The pressure at P1 is 760 Torr because it is open to atmospheric ambient pressure. The method for evaluating the error bars is described in Section III.D. As explained in Section I, the true pressures are lower than the inaccurately estimated pressures obtained by this method.

C. Pressure Estimation Using Dynamic Calibration

The following four sequential steps describe how to process the measured data and estimate the attained pressures (Fig. 2b).

The first step is to obtain the regression equations for mapping the responses of each measured Pirani gauge to that of the reference Pirani gauge (Fig. 6a–c), using the static calibration data (Fig. 5a). Since P1 is the reference Pirani gauge, each of the responses of P54, P99, and P162 is scaled to that of P1. For each regression equation with the offset of zero, the first-order coefficients are 0.9646 for P54, 0.9905 for P99, and 1.0179 for P162. The values of R^2 for mapping P54, P99, and P162 to P1 are 0.9972, 0.9980, and 0.9980, respectively. As can be seen in the plots of the scaled responses of the measured Pirani gauges and the reference Pirani gauges

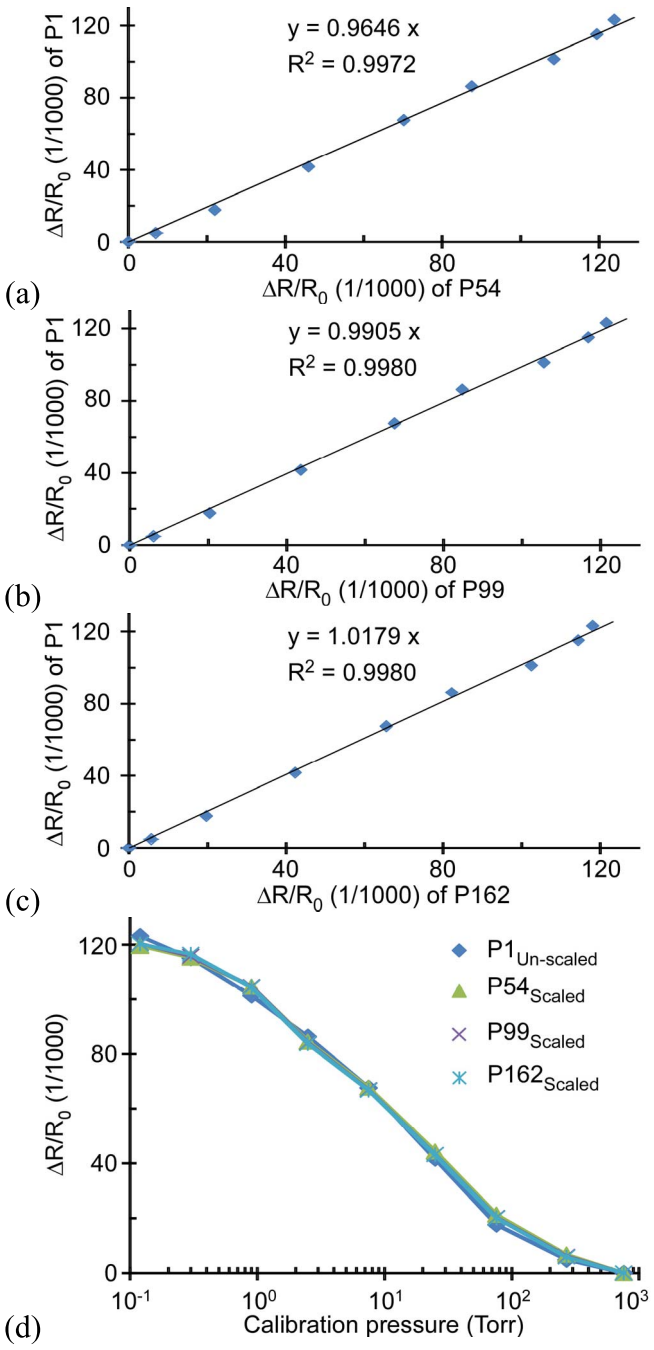

Fig. 6. Mapping of the Pirani gauges, P54, P99, and P162 to the reference Pirani gauge, P1, using linear regression. (a) The linear regression fit between P1 and P54. (b) The linear regression fit between P1 and P99. (c) The linear regression fit between P1 and P162. (d) Responses of each Pirani gauge after mapping, using regression equations, as indicated in (a–c).

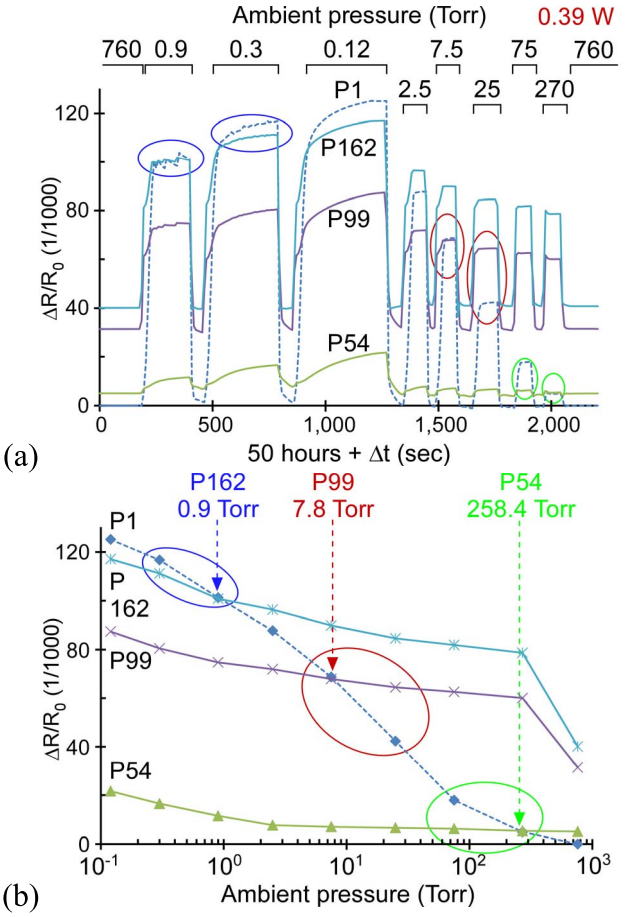

Fig. 7. Determining the equalization pressures of each Pirani gauge. (a) Scaled dynamic calibration plots; the ambient pressure is rapidly varied from 760 Torr to 0.1 Torr at about half-decade pressure intervals. (b) The equalization pressures are determined, as indicated by the dotted arrow lines between two bounding values of ambient pressure. Blue circles are for P162, red circles for P99, and green circles for P54.

(Fig. 6d), the deviations of the fractional changes in resistance with pressure are smaller than those in Fig. 5a.

The second step is to apply the linear regression equations obtained by the first step to the measured dynamic calibration plots. The dynamic calibration plots provide equalization pressures at half-decade intervals from 0.12 Torr to 760 Torr. To ensure that the pressure levels in each stage are in a steady state (Fig. 7a), the dynamic calibration is performed after 50 hours of Knudsen pump operation. The steady state response of P1 before modulation is zero in the dynamic calibration plots. During modulation, the temporal response of P1 represents the varying ambient pressure, whereas the temporal responses of P54, P99, and P162 represent both interior pressure and exterior varying ambient pressure. The response of P1 reflects the ambient pressure, and matches the static calibration. However, the plots of P54, P99, and P162 in Fig. 7a have been corrected, using the regression equations.

The third step is to determine the pressures within the Pirani gauges. As the ambient is rapidly modulated from the original value (which is 760 Torr in this case), the response of P1 is compared to those of P54, P99, and P162. Measurements are taken at the end of each modulation in order to provide the maximum settling time for each reading. The modulated ambient value at which P1 indicates pressure that is higher than the mapped response of any Pirani gauge represents the lower bound of the pressure at that gauge. Similarly, the modulated ambient value at which P1 is lower than the mapped value of any gauge represents the upper bound of the pressure at that gauge (Fig. 7a). The equalization pressure of each gauge is calculated using interpolation between these two bounding

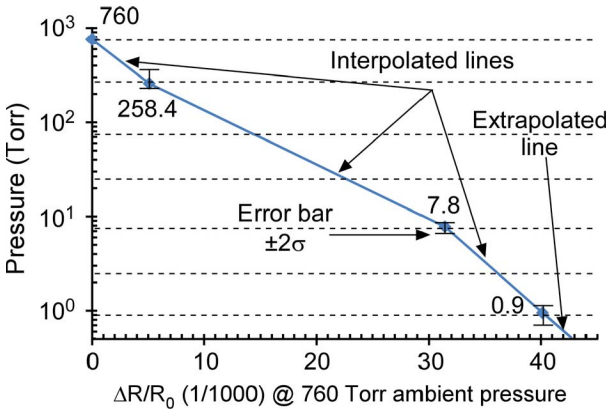

Fig. 8. The generalized relation of pressure as a function of $\Delta R/R_0$ when the ambient pressure is 760 Torr, obtained by dynamic calibration. The isolated points indicate the equalization pressures (Fig. 7b). The solid line indicates interpolations and extrapolations between the neighboring, isolated points, for approximately determining the pressures from any measured $\Delta R/R_0$. The horizontal dotted lines indicate the modulated ambient pressures for dynamic calibration.

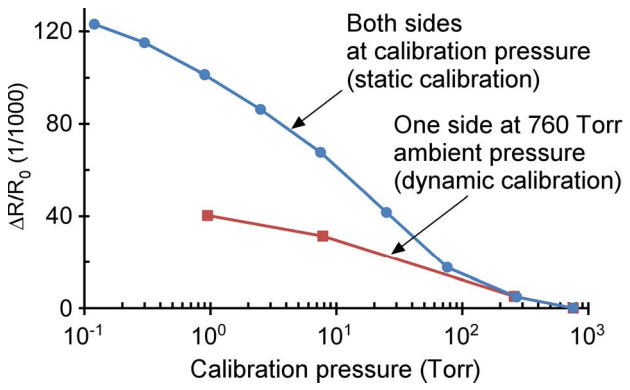

Fig. 9. The difference in fractional changes in the resistance of a Pirani gauge from static and dynamic calibration methods. The solid circles are obtained by static calibration. The solid squares are obtained by dynamic calibration for 760 Torr ambient.

pressures (Fig. 7b). For P162, the upper bound pressure, at which the response of P1 is lower than that of P162, is 0.9 Torr. The lower bound pressure, at which the response of P1 is higher than that of P162, is 0.3 Torr. For P99, two bounding pressures are 25 Torr and 7.5 Torr. For P54, two bounding pressures are 270 Torr and 75 Torr. The equalization pressures are ≈0.9 Torr for P162, ≈7.8 Torr for P99, and ≈258.4 Torr for P54.

The final, fourth step is to generalize the correlation of pressure and fractional change in resistance at the specific ambient pressure. Using the equalization pressures determined in the third step, any value of $\Delta R/R_0$ provided by the Pirani gauges can be mapped to a calibrated value of interior pressure. This value is determined using the closest points from the set 760 Torr, 258.4 Torr, 7.8 Torr, and 0.9 Torr and the corresponding $\Delta R/R_0$ of 0, 4.3×10^{-3}, 28.2×10^{-3}, and 37.7×10^{-3}, respectively (Fig. 8). However, this calibration is valid only for an exterior ambient pressure of 760 Torr. For other values of ambient pressure, the rapid pressure modulation and the second, third, and fourth steps of the procedure must be repeated (Fig. 2b). The method for evaluating the error bars is described in Section III.D.

Figure 9 compares the fractional change in resistance as a function of pressure obtained by dynamic calibration (Fig. 8) to that obtained by static calibration (Fig. 5a). As the pressure is reduced, dynamic calibration shows smaller fractional changes in resistance than static calibration.

D. Typical Errors in Calibration

The two dominant sources of error are analyzed: the repeatability of Pirani gauge sensors and the mapping of the Pirani responses using linear regression. These are used to calculate the standard deviation, σ, of the calibrated response. The uncertainty is represented by an error bar that indicates a range of $\pm 2\sigma$ (indicating a total span of 4σ), which correspond to a 95.4% confidence interval for normal (Gaussian) distribution [29].

The repeatability of the sensor is a source of error for the static and dynamic calibration. The output may vary because of the measurement tools or human factors. Error bars that identify the possible readout fluctuation can be defined for each measurement of the Pirani gauge. To evaluate this uncertainty, one Pirani gauge is repeatedly measured, using identical measurement tools, test chamber, and operator method, over a period of time. Using the repeated measurements of the $\Delta R/R_0$, the mean values and the error bars for $\pm 2\sigma$ are plotted for a range of calibration pressures (Fig. 10a). In a preliminary sample set of 6 measurements, the highest value of the standard deviation, σ, was 1.6×10^{-3}, at 0.12 Torr. The $\pm 2\sigma$ error bars in $\Delta R/R_0$ are converted into the error bars in pressure by using the two closest neighboring calibration points, using Eq. (7). Here, $(\Delta R/R_0)_{m,S}$ is replaced by $[(\Delta R/R_0)_r \pm 2\sigma]$ and $P_{m,S}$ by the resulting pressure. The resulting residual errors in pressure, ΔP_E, for the calibration pressure of ≈30 Torr are −3 Torr and +3 Torr, which are indicated as the error bar for the pressure at P162, obtained by static calibration (Fig. 5b).

Another source of error is the linear regression performed for dynamic calibration. To estimate this, the responses of multiple Pirani gauges are collected, using identical calibration pressures, measurement tools, test chamber, and operator method. Then, each response is mapped by linear regression to the mean response at every pressure – i.e., the mean is assumed to be the reference response. For a preliminary data set with 12 Pirani gauges, the first order coefficients, as shown in Eq. (9), were 0.9482, 0.9152, 0.9397, 0.9657, 0.9482, 0.9152, 0.9657, 1.1412, 1.0766, 1.0795, 1.09121, and 1.0818. The mean and the error bars for $\pm 2\sigma$ are plotted, with varying calibration pressure (Fig. 10b). The highest σ value in $\Delta R/R_0$ was 1.4×10^{-3} at the pressure of 0.9 Torr. This error is assumed to be representative of the errors due to linear regression in dynamic calibration.

The two sources of error are uncorrelated, so the total error, E_{1+2}, is [8], [30]:

$$E_{1+2} = \sqrt{E_1^2 + E_2^2} \tag{10}$$

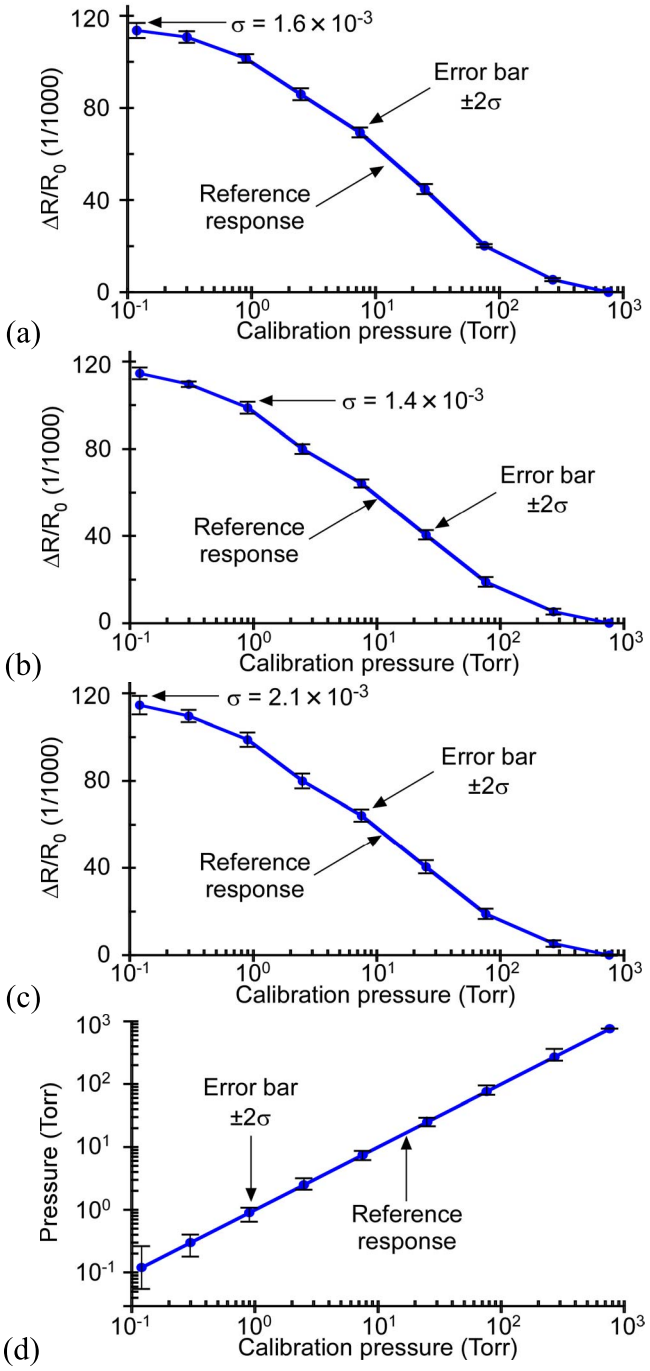

Fig. 10. Error source analysis for static and dynamic calibration methods. (a) From the repeatability of a Pirani gauge, in $\Delta R/R_0$ as a function of calibration pressure, measured with static calibration method. (b) From the mapping of the measured Pirani gauge to the reference Pirani gauge with linear regression. (c) The combined errors from (a) and (b). (d) The combined errors from (a) and (b) are converted to residual errors in pressure at each calibration pressure. In (a–c), only the highest values in σ are indicated.

where the subscripts *1* and *2* indicate two independent variables, E_1 is the standard deviation from the repeatability of responses of each Pirani gauge and E_2 is the standard deviation from the mapping of the response of the measured Pirani gauge to that of the reference gauge with linear regression. The total error is plotted in Fig. 10c. The highest value of the total error in $\Delta R/R_0$ is 2.1×10^{-3} at the calibration pressure of 0.12 Torr. The resulting residual errors in pressure, ΔP_E, for the calibration pressure of 0.9 Torr are -0.2 Torr and $+0.2$ Torr (Fig. 10d); these errors are indicated as the error bar for the pressure at P162, obtained by dynamic calibration (Fig. 8).

IV. Discussion and Conclusion

The Knudsen pump example demonstrates that dynamic calibration can be significantly more accurate than conventional static calibration for certain type of devices. The pressure of P162 was 30 Torr by static calibration (Fig. 5b) and 0.9 Torr by dynamic calibration (Fig. 7b). As the interior pressure decreases, the response of a Pirani gauge that has one side exposed to ambient pressure becomes smaller than that of a Pirani gauge for which both interior and exterior are both at the same pressure (Fig. 9). A significant contribution to this effect is due to the mechanical deflection of the supporting membrane that contacts the bump surface at the sense gap (Fig. 3d). As a result, the smaller fractional change in resistance is mapped to higher pressure than the true value. In dynamic calibration, this error is removed by modulating the ambient pressure around the interior pressure of the Pirani gauge until the responses of both gauges are equal indicating that the supporting membrane is detached from the bump surface.

It is evident from Fig. 7a that, when the ambient pressure is returned to 760 Torr after modulation, each $\Delta R/R_0$ returns back to its initial value. The pressure in the sense gaps in stages 55, 99, and 162, located upstream and far from the OUT port do not respond to rapid variations in ambient pressure. The effects of the rapid variations in ambient pressure on those interior pressures can be ignored. Therefore, the equalization pressures in dynamic calibration are valid.

One transient response shown in the dynamic calibration plots (Fig. 7a) is a large increase in the responses of P99 and P162 when the ambient pressure changes from 760 Torr to 0.9 Torr. This is caused by the supporting membrane detaching from the bump surface resulting in a large change in $\Re_{sg}$. After detaching, different ambient pressures, such as 0.9 Torr, 0.3 Torr, and 0.12 Torr, are expected to cause negligible changes in the responses. This is because the pressures in the sense gaps are unchanged and $\Re_{sg}$ is insensitive to changes in membrane deflection at low pressure in the range 1–10 Torr, where $\lambda \gg g$, as anticipated by Eq. (4).

After detaching, the responses of P99 and P162 increase in two ways: 1) from each successive step, 760 Torr to 0.9 Torr, 760 Torr to 0.3 Torr, and 760 Torr to 0.12 Torr, the responses show an initial noticeable increase; and 2) within each modulation step the responses show a gradual increase (Fig. 7a). These responses after detaching, which are unexpected from changes in membrane deflection, result from the combined effects of the Knudsen pump heater, which slowly increases pump chip temperature as ambient pressure decreases, and the time it takes for the calibration pump, ≈23 cfm, to achieve full vacuum (>17 s). However, these two effects affect all Pirani gauges equally without

changing the found equalization pressures. Therefore, the equalization pressures in dynamic calibration are valid.

The error contributed by measurement uncertainty and the regression model is relatively small near atmospheric pressure, but significant at low pressures, as shown in Fig. 10d. The small sensitivity of $\Delta R/R_0$ at low pressure relative to that at higher pressure amplifies the impact of errors in $\Delta R/R_0$, resulting in larger equivalent errors in pressure, especially at 0.12 Torr. These errors may be reduced by increasing the input current to the Pirani gauges at low pressures.

In summary, dynamic calibration has been investigated for the pressure estimation of the pressure modulating devices, with the integrated Pirani gauges. It provides superior accuracy to static calibration by accommodating the impact of the exterior ambient pressure, which is different from the interior pressures of the evacuated stages. The dynamic method is used to determine the interior pressure by rapid modulation in ambient pressure. Using four sequential steps for processing the calibration data, more accurate estimates for the interior pressures are obtained. For the sample Knudsen pump that is experimentally evaluated, the upstream pressure is 0.9 Torr, with a 95.4% confidence interval from 0.7 Torr to 1.1 Torr, assuming normal (Gaussian) distribution. In comparison, static calibration suggests the pressure of 30 Torr, with a 95.4% confidence interval from 27 Torr to 33 Torr.

APPENDIX A

In the dynamic calibration method, the responses of the Pirani gauges to be measured and calibrated could be different from the reference gauge even at the equalization pressure because of fabrication process-induced variations in the two gauges. For compensating such differences, the response of the test gauge is mapped to that of the reference gauge, using linear regression. This appendix justifies the use of linear regression by showing that the responses with pressure change, $\Delta R/R_0$, are linearly related between gauges. Two cases for the process-induced variations are analyzed: variation in the baseline electrical resistance, R_0; and variation in the thermal resistances.

A. Variation in R_0

The unheated resistance, R_0, varies typically from 130 Ω to 150 Ω, even within one Knudsen pump. Using Eq. (6), if the 2nd term on the right side is ignored for simplicity by assuming that $\Re_{th}$ at low pressure values is much larger than $\Re_{th,Ref}$, the ratio of $\Delta R/R_0$ between two Pirani gauges can be simply stated as the following Taylor series expansion:

$$\frac{(\Delta R/R_0)_m}{(\Delta R/R_0)_r} = \gamma\left\{1-(1-\gamma)(\Delta R/R_0)_r + (1-\gamma)^2(\Delta R/R_0)_r^2\ldots\right\} \quad \text{(A.1)}$$

where the subscript m indicates the Pirani gauge of interest, the subscript r indicates the reference Pirani gauge and γ is the proportionality constant, defined as $R_{0,m}/R_{0,r}$. By substituting $(\Delta R/R)_r$ with 0.12, which is a typical maximum value in the test of Pirani gauges that are further described in Section III, and γ with 0.87, which is the ratio of 130 Ω to 150 Ω, the 2nd order and 3rd order terms become 1.6% and 0.02% of the 1st order term, respectively. Because the non-linear terms are relatively small, the relation between two Pirani gauges can be regarded as approximately linear.

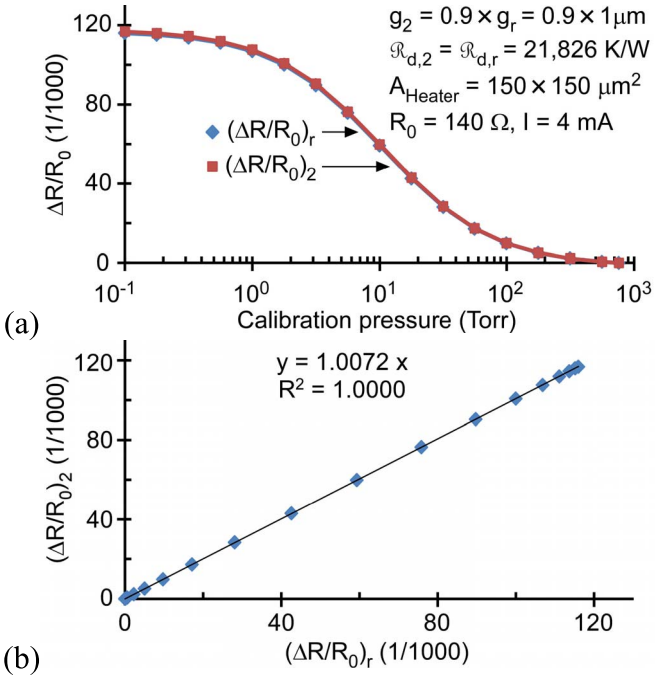

Fig. A.1. The relation between the calculated responses of two hypothetical Pirani gauges, with varying calibration pressures from 760 Torr to 0.1 Torr. (a) The responses of two hypothetical Pirani gauges as a function of calibration pressure. (b) The linear regression fit of the responses of two hypothetical Pirani gauges. Subscripts r and 2 indicate two Pirani gauges. The sense gap of the Pirani gauge 2, g_2, is assumed to be smaller by 10% than that of the reference Pirani gauge, g_r, due to the process-induced variation in sacrificial material for the sense gap.

B. Variation in $\Re_{sg}$ and $\Re_d$

The process-induced variations from $\Re_{sg}$ and $\Re_d$ are evaluated separately. Consider a hypothetical situation in which the Pirani sense gap is 1 μm, the area of the heater, A_{heater}, in Eq. (3-4) is 150 × 150 μm^2, and the value of $\Re_d$ is 21,826 K/W. These values are representative of the Knudsen pump example that is described in Section III. This hypothetical Pirani gauge, denoted as the reference gauge, is compared with another, denoted as gauge 2, in which the sense gap is 10% smaller. As shown in Fig. A.1, the pressure responses of both devices are almost identical, and the relationship between the fractional changes in resistance $(\Delta R/R_0)_2$ and $(\Delta R/R_0)_r$ can be represented by a straight line with a slope of 1.0072. This fit (Fig. A.1b) has an R^2 value of 1.0000 over the pressure range of 0.1 Torr to 760 Torr, indicating that a linear regression model can be used for mapping of the response of a Pirani gauge to that of the reference Pirani gauge in the same chip. Another hypothetical case, in which the thickness of the supporting membrane is increased by 10%, thereby reducing $\Re_d$, is shown in Fig. A.2. Once again, the relation between $(\Delta R/R_0)_3$ and $(\Delta R/R_0)_r$ is approximately

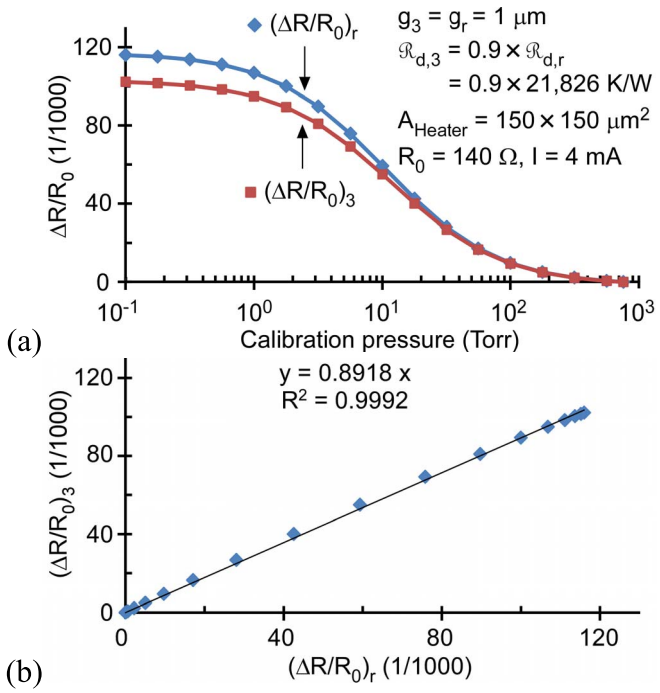

Fig. A.2. The relation between the calculated responses of two hypothetical Pirani gauges, with varying calibration pressures from 760 Torr to 0.1 Torr. (a) The responses of two hypothetical Pirani gauges as a function of calibration pressure. (b) The linear regression fit of the responses of two hypothetical Pirani gauges. Subscripts *r* and *3* indicate two Pirani gauges. The $\Re_{d,3}$ value are assumed to be smaller by 10% than the $\Re_{d,r}$ value, due to the process-induced variation in thickness for supporting membrane.

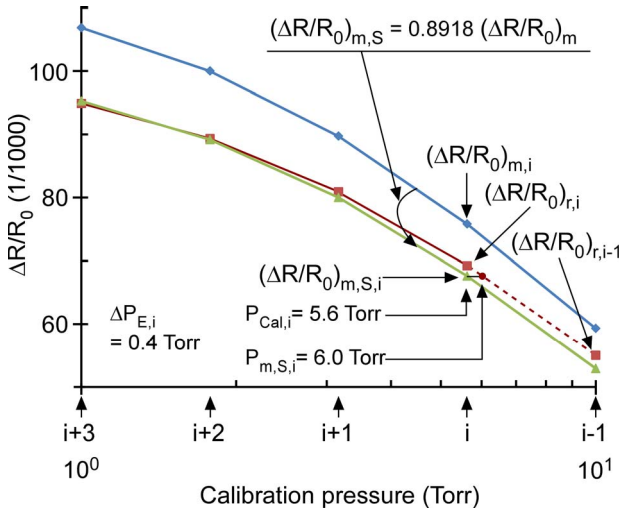

Fig. B.1. An illustrative example of the mapping of the measured Pirani gauge to the reference Pirani gauge and the resulting residual error in pressure, using the hypothetical data in Fig. A.2. The values of $(\Delta R/R_0)_m$ are linearly transformed to those of $(\Delta R/R_0)_{m,S}$ with linear regression model, as indicated in this graph, and the discrepancies with $(\Delta R/R_0)_r$ are translated into the residual errors in pressure, ΔP_E.

linear, as evidenced by the R^2 value of 0.9992 and slope of 0.8918, over the pressure range of 0.1 Torr to 760 Torr. In practice, the process induced variations are even lower because the variation in sense gap and supporting membrane thickness is generally <3% rather than the variation of 10% assumed in the hypothetical examples. The modest nature of the variation is supported by the small size of the device; for the Knudsen pump, the die size is 12 × 15 mm^2. Therefore, the relation between nearby Pirani gauges can be assumed to be linear.

Appendix B

An example of the linear transformation of the response of a measured Pirani gauge to the equivalent response of the reference pressure gauge is illustrated as follows. Using the hypothetical data in Fig. A.2, the un-scaled value of 5.6 Torr (i.e., $P_{Cal,i}$ of 5.6 Torr) is transformed to the scaled value of 6.0 Torr. As illustrated in Fig. B.1, first, the $(\Delta R/R_0)_{m,i}$ value is linearly transformed to the $(\Delta R/R_0)_{m,S,i}$ value, using Eq. (10). Second, the $(\Delta R/R_0)_{m,S,i}$ value is converted to the $P_{m,S,i}$ value of 6.0 Torr by finding the horizontal intercept from $(\Delta R/R_0)_{m,S,i}$ to the interpolated curve for $(\Delta R/R_0)_r$, which is represented by the red dotted line in Fig. B.1. This process, which is the graphical equivalent of solving Eq. (7), results in a residual error in pressure of 0.4 Torr.

Acknowledgment

The authors thank Dr. N. Gupta for his contribution to test setup and characterization of the thermal properties of Ti/Pt metal resistors. Facilities used for this research include the Lurie Nanofabrication Facility (LNF) operated by the Solid-State Electronics Laboratory (SSEL) and the University of Michigan.

References

[1] H. V. Ubisch, "On the conduction of heat in rarefied gases and its manometric application. I," *Appl. Sci. Res.*, vol. 2, no. 1, pp. 364–430, 1951.

[2] H. V. Ubisch, "On the conduction of heat in rarefied gases and its manometric application. II," *Appl. Sci. Res.*, vol. 2, no. 1, pp. 403–430, 1951.

[3] S. Wilfert and C. Edelmann, "Miniaturized vacuum gauges," *J. Vacuum Sci. Technol. A*, vol. 22, no. 2, pp. 309–320, 2004.

[4] A. W. van Herwaarden and P. M. Sarro, "Double-beam integrated thermal vacuum sensor," *J. Vacuum Sci. Technol. A*, vol. 5, no. 4, pp. 2454–2457, 1987.

[5] C. H. Mastrangelo and R. S. Muller, "Microfabricated thermal absolute-pressure sensor with on-chip digital front-end processor," *IEEE J. Solid-State Circuits*, vol. 26, no. 12, pp. 1998–2007, Dec. 1991.

[6] P. K. Weng and J. Shie, "Micro-Pirani vacuum gauge," *Rev. Sci. Instrum.*, vol. 65, no. 2, pp. 492–499, 1994.

[7] B. C. S. Chou and J.-S. Shie, "An innovative Pirani pressure sensor," in *Proc. 9th Int. Conf. Solid-State Sensors, Actuat. Microsyst.*, 1997, pp. 1465–1468.

[8] R. E. Ellefson and A. P. Miiller, "Recommended practice for calibrating vacuum gauges of the thermal conductivity type," *J. Vacuum Sci. Technol. A*, vol. 18, no. 5, pp. 2568–2577, 2000.

[9] B. H. Stark, Y. Mei, C. Zhang, and K. Najafi, "A doubly anchored surface micromachined Pirani gauge for vacuum package characterization," in *Proc. 16th IEEE Int. Conf. MEMS*, Jan. 2003, pp. 506–509.

[10] J. Chae, B. H. Stark, and K. Najafi, "A micromachined Pirani gauge with dual heat sinks," *IEEE Trans. Adv. Packag.*, vol. 28, no. 4, pp. 619–625, Nov. 2005.

[11] M. Doms, A. Bekesch, and J. Mueller, "A microfabricated Pirani pressure sensor operating near atmospheric pressure," *J. Micromech. Microeng.*, vol. 15, no. 8, pp. 1504–1510, 2005.

[12] J. Mitchell, G. R. Lahiji, and K. Najafi, "An improved performance poly-Si Pirani vacuum gauge using heat-distributing structural supports," *J. Microelectromech. Syst.*, vol. 17, no. 1, pp. 93–102, Feb. 2008.

[13] B. Xiao, T. Dong, E. Halvorsen, Z. Yang, Y. Zhang, N. Hoivik, D. Gu, N. M. Tran, and H. Jakobsen, "Integrated micro Pirani gauge based hermetic package monitoring for uncooled VO_x bolometer FPAs," *Microsyst. Technol.*, vol. 17, no. 1, pp. 115–125, 2011.

[14] F. Santagata, E. Iervolino, L. Mele, A. W. van Herwaarden, J. F. Creemer, and P. M. Sarro, "An analytical model and verification for MEMS Pirani gauges," *J. Micromech. Microeng.*, vol. 21, no. 11, pp. 115007-1–115007-7, 2011.

[15] M. Doms and J. Muller, "Design, fabrication, and characterization of a micro vapor-jet vacuum pump," *ASME J. Fluids Eng.*, vol. 129, no. 10, pp. 1339–1345, 2007.

[16] N. Gupta, S. An, and Y. Gianchandani, "A Si-micromachined 48-stage Knudsen pump for on-chip vacuum," *J. Micromech. Microeng.*, vol. 22, no. 10, pp. 105026-1–105026-8, 2012.

[17] S. An, N. K. Gupta, and Y. B. Gianchandani, "A Si-micromachined 162-stage two-part Knudsen pump for on-chip vacuum," *J. Microelectromech. Syst.*, to be published, DOI: 10.1109/JMEMS.2013.2281316.

[18] K. Kadoya, N. Matsunaga, and A. Nagahima, "Viscosity and thermal conductivity of dry air in the gaseous phase," *J. Phys. Chem. Reference Data*, vol. 14, no. 4, pp. 947–970, 1985.

[19] M. Saidi and R. H. Abardeh, "Air pressure dependence of natural-convection heat transfer," in *Proc. WCE*, Jul. 2010, pp. 1–4.

[20] H. Kim, A. A. Astle, K. Najafi, L. P. Bernal, and P. D. Washabaugh, "A fully integrated high-efficiency peristaltic 18-stage gas micropump with active microvalves," in *Proc. 20th IEEE Int. Conf. MEMS*, Jan. 2007, pp. 127–130.

[21] H. Kim, W. Steinecker, S. Reidy, G. Lambertus, A. Astle, K. Najafi, E. Zellers, L. Bernal, P. Washabaugh, and K. Wise, "Micropump-driven high-speed MEMS gas chromatography system," in *Proc. 14th Int. Conf. Solid-State Sensors, Actuat. Microsyst.*, 2007, pp. 1505–1508.

[22] J. Liu, N. K. Gupta, K. D. Wise, Y. B. Gianchandani, and X. Fan, "Demonstration of motionless Knudsen pump based micro-gas chromatography featuring micro-fabricated columns and on-column detectors," *Lab Chip*, vol. 11, no. 20, pp. 3487–3492, 2011.

[23] S. D. Senturia, *Microsystem Design*, Norwell, MA, USA: Kluwer, 2001, pp. 278–282.

[24] K. Stephan and A. Laesecke, "The thermal conductivity of fluid air," *J. Phys. Chem. Reference Data*, vol. 14, no. 1, pp. 1227–1234, 1985.

[25] E. R. Grilly, W. J. Taylor, and H. L. Johnston, "Accommodation coefficients for heat conduction between gas and bright platinum, for nine gases between 80 °K (or their boiling points) and 380 °K," *J. Chem. Phys.*, vol. 14, no. 7, pp. 435–440, 1946.

[26] W. G. Vincenti and C. H. Kruger, *Introduction to Physical Gas Dynamics*, Melbourne, FL, USA: Krieger, 1975, pp. 12–15.

[27] A. Al-Azzawi, *Photonics: Principles and Practices*. Boca Raton, FL, USA: CRC Press, 2006.

[28] W. J. Smith, *Modern Optical Engineering*, 4th ed. New York, NY, USA: McGraw-Hill, 2007, pp. 14–16.

[29] E. Kreyszig, *Advanced Engineering Mathematics*, 9th ed. New York, NY, USA: Wiley, 2006, pp. 1049–1057.

[30] S. Bell, *A Beginner's Guide to Uncertainty of Measurement*. New York, NY, USA: Crown, 1999.

Seungdo An (S'12–M'13) received the B.S. and M.S. degrees in chemistry from Korea University, Seoul, Korea, in 1995 and 2003, respectively. He worked at Samsung, Korea, from 1995 to 2010. At Samsung, he was involved in various MEMS projects, including micro gyroscope, micro magnetometer, and laser optical modulator/display. He was a Visiting Researcher at the Esashi Laboratory, Tohoku University, Sendai, Japan, in 1996. Since 2010, he has been pursuing the Ph.D. degree in electrical engineering at the University of Michigan, Ann Arbor, MI, USA, with a focus on MEMS. His academic advisor is Prof. Gianchandani.

His research interests are monolithic Knudsen vacuum pumps for micro gas chromatographs and micro mass spectrometers.

Yogesh B. Gianchandani (M'85–SM'05–F'10) is a Professor at the University of Michigan, Ann Arbor, MI, USA, with a primary appointment in the Electrical Engineering and Computer Science Department and a courtesy appointment in the Mechanical Engineering Department. He serves as the Director for the Center for Wireless Integrated MicroSensing and Systems (WIMS^2).

Dr. Gianchandani's research interests include all aspects of design, fabrication, and packaging of micromachined sensors and actuators (http://www.eecs.umich.edu/∼yogesh/). He has published about 300 papers in journals and conferences, and has about 35 U.S. patents issued or pending. He was a Chief Co-Editor of *Comprehensive Microsystems: Fundamentals, Technology, and Applications,* published in 2008. From 2007 to 2009, he also served at the National Science Foundation, as the Program Director for Micro and Nano Systems within the Electrical, Communication, and Cyber Systems (ECCS) Division. Dr. Gianchandani is a Fellow of the IEEE.